Characterization of Pt-doped SnO_2 catalyst for a high-performance micro gas sensor

Naoyoshi MURATA[1,2], Takuya SUZUKI[1], Makoto KOBAYASHI[1], Fumiaki TOGOH[1] , and Kiyotaka ASAKURA[3]

[1] Corporate R & D Headquarters, Fuji Electric Co., Ltd., Tokyo 191-8502, Japan
[2] Department of Quantum Science and Engineering, Graduate School of Engineering, Hokkaido University, Sapporo 001-0021, Japan.
[3] Catalysis Research Center, Hokkaido University, Sapporo 001-0021, Japan

Keywords:
Methane sensor, high performance, Platinum-doped tin dioxide, solid solution structure

Abstract

The atomic scale structure and its dependence on Pt concentration of a Pt-doped SnO_2 (Pt/SnO_2) thin film produced by a sputter-deposition method was investigated, which showed a high-performance methane gas sensor. Extended X-ray absorption fine structure (EXAFS) and X-ray diffraction (XRD) analyses showed that Pt/SnO_2 has a rutile structure similar to SnO_2 crystals at less than 10 at% Pt where the Pt ion was located at the Sn position in the rutile structure. There was no evidence that Pt metal clusters were formed in the Pt/SnO_2 films. The Pt/SnO_2 structure became amorphous at greater than 11 at% Pt. We found a good correlation between the methane activity and local structure of Pt.

1. Introduction.

The use of natural gas is increasing because of the ease supply and more eco-friendly energy source. Safety measures against the leak are left for further development. Actually in 2010 there were 665 cases of gas leakage reported and more than 50 explosions occurred in Japan, 60 % of which took place in residential use.[1] Thus the wide use of the gas sensor in household is strongly required. SnO_2 has been widely utilized for gas sensors because its conductivity varies with the partial pressures of oxygen and reductive gases.[2,3] The O defect in the SnO_2 gives n-type electroconductivity and the amount of O defect is controlled by the reaction with O_2 and

reductive gases. The SnO_2 sensor requires high operation temperatures, which are necessary for the reaction between the SnO_2 and gases(O_2 or reductive gases). External power-driven type SnO_2 sensors have been developed to date; however, to increase the number of gas sensors employed in households, battery-driven type or cordless model is in demand for their appearance and ease of installation. Battery-driven sensors should have lifetimes longer than 5 years and thus sensors with low power consumption and high selectivity for methane, which is a main component of natural gas, should be developed. Therefore, the current strategy is to miniaturize the sensor for a reduction in energy consumption and to enhance sensor activity by the addition of metal catalysts. Suzuki et al. developed a SnO_2 thin film produced using a microelectromechanical system (MEMS) method to achieve miniaturization of the gas sensor and reduce the power consumption.[4,5] Yamazoe et al. and Labeau et al. studied the effects of noble metal additives(Pt , Pd) on SnO_2 gas sensors and demonstrated that the metal addition enhances the sensitivities.[6,7] Recently we found that 5-9 at % Pt-doped SnO_2 (Pt/SnO_2) thin film prepared by a cosputtering method enhances the methane sensor sensitivity and reduces the operating temperature of the SnO_2 sensor device, which could provide a new means to realize a low power consumption gas sensor by the combination of MEMS-miniaturization technique.[8,9,10] The sensor can detect methane for more than 5 years at levels down to 12500 ppm, which is 1/4 of the explosion limit (53000 ppm) for methane. However, the mass production of the high-performance sensors requires further understanding of the atomic structure of the Pt/SnO_2 thin film and the enhancement mechanism by Pt doping. Two possible mechanisms were proposed to explain the enhancement of gas sensing by noble metal additives such as Pt and Pd; the charge transfer effect and the spillover effect.[11]

The electronic effects take place in noble metal oxide-promoted SnO_2 where electron transfers from SnO_2 to noble metal oxide and depletion layer is formed at the interface. The reaction of the PdO or PtO_2 with the gas modifies the thickness of electron-depleted layers in SnO_2 lattice.

Spillover of reducing adsorbates from metallic clusters to the SnO_2 enhances sensitivity.[11,12] Noble metal particles activate hydrogen and hydrocarbons on their surfaces. The activated species(hydrogen or hydrocarbons) are supplied or spilled over to the SnO_2 surface to react with pre-adsorbed oxygen atoms more easily. Consequently, SnO_2 is enhanced in its sensor sensitivity.

In the previous literature, the characterization of 0.2-12 at % Pt/SnO_2 supported the both models by detecting two kind of Pt states, oxidized Pt and Pt metal aggregates depending on the atmosphere and Pt concentration.[1,13-15] On the other hand very

recently state-of-art high resolution fluorescence EXAFS (HRFEXAFS) techniques on the real gas sensor have suggested a quite different model where the Pt ion is located at the Sn position in the rutile structure on Pt/SnO_2.[16,17] However the information derived from the HRFEXAFS was limited to the concentration as low as 0.2 wt% which is lower than the Pt content in our highest performance sample. In order to reveal the structure of Pt/SnO_2 and its mechanism for high performance, we carried out comprehensive studies on Pt/SnO_2 thin film in a wide concentration range using various characterization techniques such as X-ray diffraction (XRD), X-ray photoelectron spectroscopy (XPS), and conventional fluorescence extended X-ray absorption fine structure (EXAFS) analyses, suggesting a different activation mechanism from spillover model or charge transfer model of Pt nanoparticle took place in the cosputtered Pt/SnO_2 thin film system.

2. Experimental

2.1. Catalyst preparation

400 nm thick Pt-doped SnO_2 thin layers (denoted as X at% Pt/SnO_2, where X indicates the atomic % of Pt) were prepared on p-type Si substrates covered with native SiO_2 film (600 nm) using a magnetron sputter-deposition method, followed by annealing at 803 K. The Pt and SnO_2 contents were controlled according to the loading ratio in the targets. Both were sputtered in the presence of 2 Pa Ar and O_2 mixed gases ($Ar:O_2$ = 8:1)with a 50 W RF power. The substrate was heated at 423 K. The final Pt concentrations in the films were determined from films dissolved in hydrochloric acid using inductively coupled plasma spectroscopy (ICP).

2.2. Characterization of the catalysis

XRD patterns were recorded using a diffractometer (Rigaku, ATX-G) with Cu Kα radiation operated at 50 kV-300 mA. XPS spectra were measured using a spectrometer (Ulvac Phi, Quantum-2000) with monochromatized-Al Kα radiation operated at 15 kV-15 mA.

Pt L_3-edge EXAFS spectra were measured using the BL-12C beamline at the Photon Factory (High Energy Accelerator Research Organization; KEK-PF) using a Si(111) double crystal monochromator in a fluorescence mode[18,19], and Sn K-edge EXAFS spectra were measured at the NW-10A beamline (KEK-PF-AR) equipped with a Si(311) double crystal monochromator also in a fluorescence mode.[20] EXAFS spectra were analyzed using REX2000 software (Ver. 2.5, Rigaku).[21-23] The backgrounds of all

EXAFS spectra were removed using a spline smoothing method with Cook and Sayers criteria and normalized according to the edge height.[24] The k^3-weighted EXAFS oscillations were Fourier-transformed to k-space over k = 14–148 nm^{-1} for the Pt L_3-edge spectra and over k = 23–144 nm^{-1} for the Sn K-edge spectra. Each peak in the Fourier transforms was filtered and inversely Fourier transformed to the k-space for the curve fitting analysis. Non-linear least-squares curve fitting was conducted using the following equations:[22]

$$k^3\chi(k) = \sum_j S_0^{\,2} \frac{k^2 N_j F_j(k)}{r_j^{\,2}} e^{-2k^2\sigma_j^{\,2}} e^{-\frac{2r_j}{\lambda_j}} \sin(2kr_j + \phi_j)$$
$$k = \sqrt{\frac{2m}{\hbar^2}(h\nu - E_o - \Delta E)} \quad , \qquad (1)$$

where S_0^2, N_j, r_j, and σ_j are the amplitude reduction factor, coordination number, bond distance, and Debye-Waller factor, of the j-th coordination shell, respectively, λ_j is the mean free path, and $F_j(k)$ and $\phi_j(k)$ are the backscattering amplitude and phase-shift functions obtained using FEFF (Ver. 8.0).[25-27] E_0 is the absorption edge energy, which was tentatively determined as the inflection points. The energy shift ΔE was adjusted during the fitting process.

The errors were estimated from Hamilton R-factor tests with a significance level over 90%:[28]

$$\mathrm{R-factor} = \frac{\sqrt{\sum_i (\chi_i^{\,\mathrm{data}}(k) - \chi_i^{\,\mathrm{fit}}(k,[\alpha]))^2}}{\sqrt{\sum_i \chi_i^{\,\mathrm{data}}(k)^2}} \,. \qquad (2)$$

2.3 Catalyst performance

The catalyst performance of the Pt/SnO_2 films was evaluated using a flow reactor (Okura Riken Co.) with a space velocity of 16800 SV [h^{-1}]. Two catalytic combustion reactions with 5000 ppm CH_4 and 5000 ppm H_2 balanced with O_2 were performed at 723 and 473 K, respectively. The products of the reaction were analyzed using gas chromatography.

3. Results and discussion.

3.1 Catalytic activity of Pt/SnO_2

Methane combustion activity and sensing activity were directly correlated. Figure 1 shows the results for the conversion of methane (723 K) and hydrogen (473 K) for Pt/SnO_2 films with Pt loading from 0 to 15 at%. Methane conversion increased gradually with increased Pt content up to 5 at% and then became saturated at 6 at% Pt followed by rapid decrease at greater than 10 at% Pt. The conversion rates of H_2 also increased with the Pt loading, and almost 100% conversion was achieved at about 9 at% Pt/SnO_2 and higher. Triangles were white line peak heights in X-ray absorption near edge spectra(XANES) discussed later. エラー! 参照元が見つかりません。 shows the dependence of the electrical resistance (R) for 9 at% Pt/SnO_2 and non-doped SnO_2 on the CH_4 and H_2 partial pressures at 723 K. The change of the R reflects the number of carrier which is accompanied with the oxygen defects. The oxygen defects were created by the reaction with the reducing gases and removed by the adsorption of oxygen.[29] The R decreased with the increase in the partial pressures (p) of hydrogen or methane, according to $R=\alpha\, p^a\, [O_2]^b$, Log-Log plot of R and p gives the value, a, as a slope. The a values for hydrogen and methane were determined to be -0.92 and -0.36, respectively, over the 9 at% Pt/SnO_2 film, while the a values over the SnO_2 film without Pt were -0.26 and -0.16, respectively. The conductivity dependence of the SnO_2 films with Pt on H_2 partial pressure was almost -1, indicating that the reaction may be diffusion-limited by the addition of Pt to enhance the activity of the surface reaction.

3.2 Crystal structure analysis of Pt/SnO_2 by XRD.

Figure 2. Electrical resistance of 9 at% Pt-doped SnO_2 and SnO_2 as a function of hydrogen (triangles) and methane (circles) concentration, Filled and open symbols are corresponding to Pt-doped SnO_2 and SnO_2, respectively. The temperature was 723 K.

Figure 3 shows XRD patterns of Pt/SnO_2 thin films with various Pt loadings. The SnO_2 thin film had a rutile structure with peaks at 26.7, 33.8, 38.3, and 52.2°, which corresponded to the (110), (101), (200), and (211) diffractions of the rutile structure, respectively. Pt/SnO_2 films with less than 10 at% Pt principally had also a rutile structure and no peaks that would indicate platinum particles were observed. However, peak broadening and peak shift were observed, which indicate modification of the SnO_2 lattice and a decrease in crystallinity due to the influence of Pt. A broad amorphous-like pattern was observed for Pt doping at 14 at%. In addition, the

diffraction peaks for Pt/SnO_2 less than 10 at% were shifted to larger angles with increased Pt loading, which indicated contraction of the rutile lattice, as shown in the panel (b) of Figure 3. The *a*- and *c*-axis parameters for the rutile structure were calculated from the XRD peak positions for each Pt concentration, as shown in Figure 4. Both the *a* and *c* axes were contracted with increasing Pt content. The Pt may have a strong interaction with the SnO_2 lattice to modify the lattice constant up to 9 at% Pt. As Pt content increases, contractions of 4.75 to 4.68 Å along the *a*-axis and 3.195 to 3.18 Å along the *c*-axis were observed, as shown in Figure 4. One possible reason for the lattice contraction is the formation of Pt particles at the SnO_2 grain boundaries, which results in compression of the SnO_2 particles. The other possibility is that most Pt atoms are substituted for Sn in the SnO_2 lattice to form a solid solution. The inclusion of Pt induces lattice disorder and results in an amorphous state at 11 at% Pt loading. To determine which of the proposed hypotheses is correct, the local Pt structures were investigated using XAFS.

3.3 XAFS analysis of Pt/SnO_2.

3.3.1 XANES spectra of Pt/SnO_2

Figure 5 shows Sn K-edge XANES spectra for the 9 at% Pt/SnO_2 sample and reference compounds. Compared with the Sn K-edge XANES spectra for SnO_2, SnO, Sn-foil, and PtSn alloy, the 9 at% Pt/SnO_2 film has a similar structure to that of SnO_2. Figure 6(a) shows magnified spectra around the Sn K-edge for SnO_2, and the 9 and 14 at% Pt/SnO_2 films. Although the absorption edge structure was similar, there was a slight shift in the edge position for the Pt/SnO_2 films shown in Fig.6(a). The Sn K-edge energies were estimated from the first inflection point and plotted as a function of the Pt loading as shown in Figure 6(b). The Sn K-edge was linearly shifted to the lower energy side with increased Pt loading. The electronic state of Sn was modified by a few percent % Pt. These results are well explained by the hypothesis that Pt is highly dispersed throughout the SnO_2 matrix and can influence the electronic state of Sn. Comparison of the electronegativities of Pt (2.2) and Sn (1.8) suggests that more electrons remain with Sn in the Pt-O-Sn system than in the Sn-O-Sn system, and hence the Sn K-edge is shifted to lower energy. Further analysis on the K-edge shift is now in progress based on the DFT calculation.

Figure 7(a) shows Pt L_3-edge XANES spectra for the Pt/SnO_2 samples and reference compounds. The white line peak heights of the 7 and 9 at% Pt/SnO_2 spectra have slightly larger intensities than that for PtO_2 and much larger than those for Pt foil and PtSn alloy. Figure 7(b) shows the dependence of the white line intensity on the Pt

concentration in Pt/SnO_2 and that for PtO_2. Low Pt loading resulted in higher peak and that for 14 at% Pt/SnO_2 was slightly smaller than that for PtO_2. The origin of the white line peak is the transition from the $2p_{3/2}$ core state to the 5d empty state; therefore, the stronger intensity suggests the presence of more empty 5d states in the Pt/SnO_2 samples with Pt content less than 10 at% than in PtO_2, while there is less d vacancy in 14 at% Pt/SnO_2. The d electrons in Pt in the SnO_2 lattice may be strongly drawn by the surrounding Sn^{4+}, which results in a stronger white line height than that for PtO_2.

3.3.2 EXAFS spectra of Pt/SnO_2

Figure 8 shows the k^3-weighted Sn K-edge EXAFS oscillations ($k^3\chi(k)$) and the Fourier transform (FT) for 9 at% Pt/SnO_2 together with several reference samples. The FT of Pt/SnO_2 was close to that of SnO_2, which indicated that the SnO_2 rutile structure was maintained in the sample. The first peak corresponds to Sn-O, while characteristic peaks that appeared in the range of 2.5–4 Å corresponded to the two Sn-Sn interactions of rutile SnO_2. Figure 9 shows the Sn K-edge $k^3\chi(k)$ and FTs for Pt/SnO_2 with various Pt content. The Pt/SnO_2 samples with the Pt content less than 9 at% had similar $k^3\chi(k)$ and FTs to those of SnO_2. The EXAFS oscillations were gradually reduced with increase of the Pt content. The peaks in the range of 2.5–4 Å disappeared in the 14 at% Pt sample by the loss of the order structure and/or the interference of Sn-Pt EXAFS oscillations to Sn-Sn EXAFS oscillations in the large Pt concentration.

Figure 10 shows Pt L_3 edge $k^3\chi(k)$ and FTs for Pt/SnO_2 samples and reference compounds. The Pt L_3-edge $k^3\chi(k)$ and FT of PtO_2 had different oscillations from those of Pt/SnO_2, which indicated the structure of Pt in Pt/SnO_2 was not PtO_2. The peak at 1–2 Å for 9 at% Pt/SnO_2 in Figure 10(b) corresponded to Pt-O, while the peaks in the range of 2.5–4 Å could be assigned to Pt-Sn or Pt-Pt.

Figure 11 shows the Pt L_3-edge $k^3\chi(k)$ and FTs for Pt/SnO_2 with various Pt content. Complex structures appeared in the high k region for the samples with less than 10 at% Pt, but the oscillations became more simple at greater than 11 at% Pt loading. Correspondingly, the peak intensities in the range of 2.5–4 Å decreased with the increase in the Pt concentration and then disappeared at 11 at% Pt.

The changes in FT and $k^3\chi(k)$ could be rationalized as follows. If Pt was located in the lattice of SnO_2, then the Pt L_3 edge should have similar $k^3\chi(k)$ and FT to those of the corresponding Sn K-edge. The FT had a similar structure to that of SnO_2 with small difference in the shape of 2.5-4 Å peaks because the Sn K-edge was located at higher energy and the resolution was worse due to life-time broadening. The increase of Pt concentration diminished the peak at 2.5–4 Å because the interference of Pt(Sn)-Pt

and Pt(Sn)-Sn interactions appeared as a result of Sn replacement with Pt. Further increase of the Pt content resulted in breakdown of the SnO_2 lattice and the formation of an amorphous structure. It was concluded that Sn atoms were substituted with Pt atoms gradually to be located at the octahedral site of the rutile at Pt content up to 10 at% and formation of the amorphous structure began at 11 at% Pt.

To obtain more detailed information on the structure, curve fitting analyses were conducted and the results were shown in Tables 1–4. First, curve fitting analyses were conducted for the first peak. Tables 1 and 2 show the results for the Pt-O and Sn-O bonds, respectively. The Pt-O distance in the Pt/SnO_2 samples was slightly shorter than that for PtO_2 and much shorter than Sn-O distance in SnO_2. The Pt-O distance was almost the same within the limit of error among the Pt/SnO_2 samples with different Pt content. The coordination number was 6.0 in 5 at% Pt/SnO_2, which indicated Pt was located in the octahedral site of the SnO_2 rutile crystal lattice. The Pt-O coordination number remained at 6 for up to 10 at% Pt and then gradually decreased with increased Pt content, probably due to the partial formation of an amorphous structure around Pt, which induced local disorder in the lattice that could not be compensated by the Debye-Waller factor. At 14 at% Pt, the Pt-O coordination number was further diminished. Table 2 shows the curve fitting result of Sn K-edge. For 5 at% Pt/SnO_2, the coordination number of Sn-O was 6 and the bond distance was about 2.05 Å. The Pt concentration dependence was not observed in the Pt/SnO_2 with Pt content up to 11 at%. However, the Sn-O coordination number was diminished at 14 at% Pt/SnO_2, probably due to the formation of an amorphous phase. It is interesting that the coordination number for Sn-O remained at 6 for 11 at% Pt/SnO_2, while that for Pt-O was slightly decreased. This may be due to the formation of an amorphous structure at 11 at% Pt only around the Pt sites while many Sn atoms remain in the crystal lattice. Then we conducted the second shell analysis of Pt L_3-edge and Sn K-edge EXAFS. However, this was quite difficult. There were at least two shells in the M-Sn (M=Pt or Sn) interaction in the rutile structure. As the Pt content increased, two more M-Pt interactions were evident and the EXAFS oscillations interfered with those of the original M-Sn interaction. Consequently, four-shell fitting analysis was required and 16 fitting parameters were necessary though the degree of freedom for the analysis was almost 17 (= $2\Delta k\Delta r/\pi$), and thus the four-shell fittings with full parameters were less reliable and quite erroneous. Two-shell fittings were first conducted for 5 at% Pt/SnO_2 for both edges where the M-Pt contributions were the least. Sn-Sn bond distances were obtained from the Sn K-edge of Pt/SnO_2 at 3.16 and 3.72 Å, which corresponded well with those in the SnO_2 (3.16 and 3.73 Å) and confirmed again that

the SnO_2 rutile structure was maintained. The local structure around Pt was obtained from Pt L_3-edge EXAFS spectra. Pt-Sn distances were found at 3.13 and 3.68 Å, which were shorter than those of corresponding Sn-Sn bond distances in the SnO_2. The curve fitting analysis again demonstrated that Pt was located in the SnO_2 lattice and the local structure of Pt was explained by the PtO_2-SnO_2 solid solution model. When the two-shell fitting of M-Sn was applied to the other Pt/SnO_2 samples (Pt content less than 11 at%), the bond distances were almost the same as those found in 5 at% Pt/SnO_2, although the M-Sn coordination numbers decreased with increase in the Pt content because the increasing contribution of M-Pt interaction was neglected and the increase in the local disorder of the SnO_2 lattice induced by Pt substitution.

In these analyses no evidence for the formation of Pt metal clusters was obtained, because good fitting results could not be obtained when the data were fitted assuming a Pt-Pt distance of 2.77 Å. EXAFS is a bulk technique and there was a possibility of the presence of Pt metal clusters on the SnO_2 surfaces. Therefore, XPS analyses were performed to determine the surface structures and state of the Pt species in Pt/SnO_2.

3.4 Surface analysis of Pt/SnO_2 by XPS.

Figure 12 shows XPS spectra of O 1s, Sn 3d, and Pt 4f in Pt/SnO_2 samples. The binding energy of Sn $3d_{5/2}$ coincided with that of the tetravalent state. The binding energy was slightly shifted to the lower energy side with Pt doping, which corresponded to the XANES results, *i.e.*, Pt does not draw as much electron in the Pt-O-Sn system as Sn does in the Sn-O-Sn system. The binding energy of Pt $4f_{7/2}$ appeared at 75.2 eV, which corresponded to Pt^{4+}.[30] A small shoulder was observed at 73.1 eV, which was more significant for the sample with Pt content greater than 11 at%. Deconvolution of the Pt 4f peak in Pt/SnO_2 was performed and the results were shown in Figure 13. There were two Pt species in SnO_2 with binding energies of $Pt4f_{7/2}$ at 75.2 and 73.1 eV, respectively. The former corresponded to Pt^{4+} while the latter indicated the presence of Pt^{2+}. A small amount of the 73.1 eV peak was detected in the samples with Pt content less than 10 at%. The ratios of the 75.2 to 73.1 eV peaks were evaluated and the results were shown in Table 5 together with the binding energies of Sn $3d_{5/2}$ and O1s. The peak ratios for 5–10 at% Pt/SnO_2 were almost 84:16. The Pt^{2+} content increased at more than 11 at% Pt. However, Pt^0 was not observed in the XPS spectra. The white line intensity of the Pt L_3 edge suggested the bulk Pt was tetravalent and the intensity decreased with Pt content greater than 11 at%, which corresponded well with the XPS observation where Pt^{2+} began to increase. Thus, the surface Pt valence state was not significantly different from that in the bulk. From both the EXAFS and

XPS results, we concluded that Pt metal was not formed even on the surface of Pt/SnO_2.

3.5 Discussion

3.5.1 Local structure of Pt species.

This work showed that no Pt nanoparticles were detected over the entire range of Pt content in Pt/SnO_2 and all measurements indicated that the Pt species was located at the Sn site in the SnO_2 lattice. Thus, Pt and SnO_2 formed a solid solution structure. These results were consistent with the reports of Weimer et al.[16] In addition, the replacement of Pt induced lattice contraction and distortion, as demonstrated from the XRD analysis. This corresponded with the smaller Pt-O distances determined from EXAFS. The lattice distortion induced vitrification of the SnO_2 crystal lattice at greater than 11 at% Pt and Pt/SnO_2 was transformed completely into an amorphous state at 14 at% Pt. This is due to the difference in the ionic radii of Pt^{4+} and Sn^{4+}; Shannon's ion radius of Pt^{4+} is 0.77 Å while that of Sn^{4+} is 0.83 Å.[31] The contraction of the lattice was larger in the *a*-axis than in the *c*-axis. EXAFS analyses indicated that the each Sn-Sn or Pt-Sn bond distance had little dependence on the Pt concentration. We inferred that more Pt-Pt interaction was present in the *ab* plane than in the *c*-axis. Considering the rutile lattice structure, Pt-Pt interaction occurred between the center and the corner site rather than that between centers along the *c*-axis. Consequently, the lattice contraction is mainly in the *ab* plane. The lattice contraction and distortion caused by Pt replacement may lead to the amorphous structure formed at 14 at% Pt/SnO_2.

3.5.2 Structure and activity

9 at% Pt/SnO_2 showed the highest activity for the CH_4 oxidation reaction. The XRD, EXAFS, and XPS results indicated that Pt was located in the SnO_2 lattice and no evidence was found for the formation of Pt or PtO nanoparticles. At higher Pt concentration, the lattice structure began to break down and in the 14 at% Pt sample, the structure was changed to an amorphous phase with little activity for CH_4 oxidation, as shown in Figure 1. Pt^{4+} and Pt^{2+} were observed in the amorphous structure, but no evidence was obtained for the formation of Pt metal clusters. Consequently, Pt^{4+} in the Sn position of the lattice was the active species for the CH_4 oxidation. The oxidation of CH_4 may proceed with the Mars-van Krevelen-like mechanism,[32] where CH_4 is oxidized using the lattice oxygen which produces oxygen defect. Oxygen defect

provides two electron or refilled by the reaction of O_2. Pt in Pt/SnO_2 prepared by the RF magnetron sputtering method effectively replaces Sn in the SnO_2 lattice, which results in a high performance for methane oxidation by the modification of lattice oxygen activity. At the same time Pt at the lattice is stable against the aggregation to large Pt nanoparticles after the long time use.

Gaidi et al. reported that Pt was in an oxidized state with a Pt-O distance of 1.96 Å and metallic state at higher Pt loading and under reductive conditions.[13] The location of Pt was seemingly outside of lattice. They also reported that the Pt was reduced to the metallic state in a reducing gas and the redox of Pt was related to its sensing properties. Other works by Lee[33] and Kappler[34] showed the presence of both oxidized and metallic Pt states and the active site structure was not clarified. Weimer et al. claimed Pt atomically dispersed in the SnO_2 lattice was active structure which generated atom/molecular adsorption sites for oxygen near the Pt atoms at the surface.[16] In the present work a high-performance sensor with long lifetime should have Pt located at the lattice point of SnO_2 which is stable upto 9 at%. At the concentration more than 10 at%, Pt/SnO_2 becomes amorphous where the Pt/SnO_2 is not active for methane gas sensing. Thus the Pt in the crystal lattice may create the active center or activate the lattice oxygen. Recently $Pt\text{-}Ce_xTi_{1-x}O_2$ exhibited high activity for CO oxidation, where the sample was prepared by a solution combustion method that resulted in Pt located in the oxide lattice.[35] Probably the oxygen atoms around the Pt were activated to take part in the redox reaction. Finally we should mention that reduced Pt metallic aggregates which are usually believed to be the origin for high activity for the oxidation reaction have nothing to do with the high performance of Pt-promoted SnO_2 sensor.

4. Conclusions

The crystal structure and catalytic properties of the Pt/SnO_2 catalyst prepared by a sputter-deposition technique for the oxidation of CH_4 and H_2 gas were investigated to evaluate the advantages of this catalyst for application in a methane gas sensor. The structure of Pt/SnO_2 was characterized using XRD, XPS, and EXAFS. Pt/SnO_2 formed a solid solution structure with the rutile crystal structure at Pt loading up to 10 at%. The catalytic activity toward methane oxidation was the highest at for 9–10 at% Pt. The CH_4 oxidation properties were lost at greater than 11 at% Pt due to structural distortion and change to an amorphous structure. However, H_2 oxidation steadily increased with the Pt loading.

5. Acknowledgment

This research was conducted with support from the “Next Generation High Reliability Gas Sensor Technical Development” project of the New Energy and Industrial Technology Developments Organization (NEDO). All EXAFS measurements were conducted at the Photon Factory, KEK as (PAC No. 2010G592, PAC No. 2012G680).

---

1 Fire and Disaster Management Agency of Japan, “Statistical Table for explosion and leakage cases by gases and hazardous chemicals in 2011” , http://www.fdma.go.jp/concern/law/tuchi2407/pdf/240731_ki183.pdf
2 G. Heiland, Sens. Actuators, 1982, **2**, 343-361.
3 N. Barsan, D. Koziej and U. Weimar, Sens. Actuators B, 2007, **121**, 18-35.
4 T. Suzuki, K. Kunihara, M. Kobayashi, S. Tabata, K. Higaki and H. Ohnishi, Sens. Actuators B, 2005, **109**, 185-189.
5 S. Tabata, K. Higaki, H. Ohnishi, T. Suzuki, K. Kunihara and M. Kobayashi, Sens. Actuators B: Chem., 2005, **109**, 190-193.
6 N. Yamazoe, Y. Kurokawa and T. Seiyama, Sens. Actuators, 1983, **4**, 283-289.
7 A. V. Tadeev, G. Delabouglise and M. Labeau, Mat. Sci. Eng. 1998, **B57**, 76-83.
8 T. Suzuki, S. Soma and T. Nagase, Fuji Electric Review, 2012, **58**, 37-40.
9 T. Suzuki, T., K.Onodera, F. Inoue, K. Tsuda, K., Jpn. Pat. JP3812215, 2006.
10 T. Suzuki, K. Onodera, F. Inoue and K. Tsuda, Jpn. Pat. JP4376093. 2009
11 N. Yamazoe, Sens. Actuators B, 1991, **5**, 7-19.
12 I. Kocemba and J. Rynkowski, Sens. Actuators B, 2011**, 155**, 659-666.
13 M. Gaidi, M. Labeau, B. Chenevier and J. L. Hazemann, Sens. Actuators B, 1998, **48**, 277-284.
14 A. Kowal, M. Li, M. Shao, K. Sasaki, M. B. Vukmirovic, J. Zhang, N. S. Marinkovic, P. Liu, A. I. Frenkel and R. R. Adzic, Nat. Mater., 2009, **8**, 325-330.
15 L. Mädler, T. Sahm, A. Gurlo, J. -D. Grunwaldt, N. Barsan, U. Weimar and S. E. Pratsinis, J. Nanopart. Res., 2006, **8**, 783-796.
16 M. Hübner, D. Koziej, M. Bauer, N. Barsan, K. Kvashnina, M. D. Rossell, U. Weimar and J. –D. Grunwaldt, Angew. Chem. Int. Ed., 2011, **50**, 2841 –2844.
17 M. Hübner, N. Bârsan and U. Weimar, Sens. Actuators B, 2012, **171-172**, 172-180.
18 M. Nomura, J. Synchrotron Radiat., 1998, **5,** 851-853.
19 M. Nomura and A. Koyama, J. Synchrotron Rad., 1999, **6**, 182-184.
20 M. Nomura, Y. Koike, M. Sato, A. Koyama, Y. Inada and K. Asakura, AIP Conf. Proc., 2007, **882**, 896-898.
21 K. Asakura, in Analysis of EXAFS in X-ray Absorption Fine Structure for Catalysts and Surfaces, ed. Y. Iwasawa, World Scientific, Singapore, 1996, p. 33.
22 T. Taguchi, AIP Conf. Proc., 2007, **882**, 162-164.
23 K. Asakura, in Polarization-dependent Total Reflection Fluorescence Extended X-ray Absorption Fine Structure and its Application to Supported Catalysis in

Catalysis Book Series, ed. J. G. Catalano, 2012, p. 281.
24 J. W. Cook and D.E. Sayers, J. Appl. Phys., 1981, **52**, 5024-5031.
25 M. Newville, J. J. Kas, J. J. Rehr, J. Phys. Conf. Ser., 2009, **190**, 012023.
26 J. J. Rehr, J. J. Kas, M. P. Prange, A. P. Sorini, Y. Takimoto and F. Vila, Compte Rendus Phys., 2009, **10**, 548-559.
27 J. J. Rehr, Radiation Phys. Chem., 2006, **75**, 1547-1558.
28 W. C. Hamilton, Acta Cryst. 1965, **18**, 502-510.
29 S. Samson and C. G. Fonsted, J. Appl. Phys., 1973, **44**, 4618-4621.
30 D. Briggs and M. P. Seah, in Practical Surface Analysis, John Wiley & Sons. Vol. 1, 2nd edition, 1993.
31 R. D. Shannon, Acta Cryst., 1976, **A32**, 751.
32 P. Mars and D. W. van Krevelen, Chemical Engineering Science, 1954, **3**, Supplement 1, 41.
33 D. -D. Lee and W. -Y. Chung, Sens. Actuators B, 1989, **20**, 301-305.
34 J. Kappler, N. Bârsan, U. Weimar, A. Dièguez, J. L. Alay, A. Romano-Rodriguez, J. R. Morante and W. Göpel, Fresenius J. Anal. Chem., 1998, **361**, 110-114.
35 T. Baidya, K. R. Priolkar, P. R. Sarode, M. S. Hegde, K. Asakura, G. Tateno, Y. J. Koike, Chem. Phys., 2008, **128**, 124711.

Table 1. Curve fitting results for Pt-O bond to Pt L_3-edge FT-EXAFS using FEFF.

Pt L_3-edge EXAFS spectra		**Curve fitting result by FEFF for Pt-O bond coordination number (CN) bond distance (r), Debye-Waller factor (σ)**				
	Pt concentration / at%	**CN**	**R / Å**	**ΔE / eV**	**σ^2 / Å ^{2}**	**R factor / %**
Pt/SnO_2	**5**	6.0 (±1)	2.005 (±0.005)	25 (0)	0.0018 (0)	1.5
	7	6.0 (±1)	2.005 (±0.005)	25 (0)	0.0018 (0)	2.6
	9	5.8 (±1)	2.005 (±0.005)	25 (0)	0.0018 (0)	3.9
	10	5.8 (±1)	2.005 (±0.005)	25 (0)	0.0018 (0)	2.6
	11	5.2 (±1)	2.005 (±0.005)	25 (0)	0.0018 (0)	5.1
	14	4.7 (±1)	2.005 (±0.005)	25 (0)	0.0018 (0)	3.9
PtO_2		6.0 (0)	2.023 (0)	25 (0)	0.0018 (0)	6.0

k range/ $Å^{-1}$ is $1.4 \leq k \leq 14.8$; r range/ $Å^{-1}$ is $1.3 \leq r \leq 1.9$; fitting space is back k space.

Table 2. Curve fitting results for Sn-O bond to Sn K-edge FT-EXAFS using FEFF.

Sn K-edge EXAFS spectra		**Curve fitting result by FEFF for Sn-O bond coordination number (CN) bond distance (r), Debye-Waller factor (σ)**				
	Pt concentration / at%	**CN**	**R / Å $^{-1}$**	**ΔE / eV**	**σ^2 / Å ^{2}**	**R factor / %**
Pt/SnO_2	**5**	6.0 (±0.3)	2.045 (±0.005)	28 (0)	0.0018 (0)	5.0
	7	6.0 (±0.3)	2.045 (±0.005)	28 (0)	0.0018 (0)	2.5
	9	6.0 (±0.3)	2.045 (±0.005)	28 (0)	0.0018 (0)	3.6
	10	6.0 (±0.3)	2.045 (±0.005)	28 (0)	0.0018 (0)	1.1
	11	6.0 (±0.3)	2.045 (±0.005)	28 (0)	0.0018 (0)	1.2
	14	3.8 (±0.3)	2.045 (±0.005)	28 (0)	0.0018 (0)	8.7
SnO_2		6.0 (0)	2.045 (±0.005)	28 (0)	0.0018 (0)	1.0

k range/ 10 Å^{-1} is $2.3 \leq k \leq 14.4$; r range/ 10 Å^{-1} is $1.3 \leq r \leq 1.9$; fitting space is back k space.

Table 3. Curve fitting result for Pt-Sn bond to Pt L_3-edge FT-EXAFS using FEFF.

Pt L_3-edge EXAFS spectra		**Curve fitting result by FEFF for Pt-Sn bond coordination number (CN) bond distance (r), Debye-Waller factor (σ)**				
	Pt concentration / at%	**CN**	**R / Å $^{-1}$**	**ΔE / eV**	**σ^2 / Å ^{2}**	**R factor / %**
Pt/SnO_2	**5**	1.3 (0)	3.13 (±0.01)	-3 (0)	0.0014 (0)	6.6
		7.0 (±0.2)	3.68 (±0.02)	5 (0)	0.0023 (0)	
	7	1.1 (±0.1)	3.12 (±0.01)	-3 (0)	0.0014 (0)	12.0
		5.1 (±0.1)	3.68 (±0.01)	5 (0)	0.0023 (0)	
	9	1.1 (±0.1)	3.12 (±0.01)	-3 (0)	0.0014 (0)	9.0
		4.8 (±0.4)	3.68 (±0.02)	5 (0)	0.0023 (0)	
	10	0.7 (±0.1)	3.14 (±0.01)	-3 (0)	0.0014 (0)	10.0
		4.7 (±0.4)	3.67 (0)	5 (0)	0.0023 (0)	
	11					
	14					

k range/ 10 Å^{-1} is $2.3 \leq k \leq 14.8$; r range/ 10 Å^{-1} is $2.2 \leq r \leq 4.0$; fitting space is back k space.

Table 4. Curve fitting result for Sn-Sn bond to Sn K-edge FT-EXAFS using FEFF.

Sn K-edge EXAFS spectra		Curve fitting result by FEFF for Sn-Sn bond coordination number (CN) bond distance (r), Debye-Waller factor (σ)				
	Pt concentration / at%	CN	R / Å $^{-1}$	ΔE / eV	σ^2 / Å ^{2}	R factor / %
Pt/SnO_2	5	1.3 (±0.1)	3.16 (±0.01)	-3 (0)	0.0014 (0)	6.4
		5.6 (±0.5)	3.72 (±0.01)	5 (0)	0.0023 (0)	
	7	1.0 (±0.2)	3.16 (±0.01)	-3 (0)	0.0014 (0)	5.7
		4.8 (±0.3)	3.72 (±0.01)	5 (0)	0.0023 (0)	
	9	0.9 (±0.1)	3.15 (±0.01)	-3 (0)	0.0014 (0)	8.2
		4.6 (±0.1)	3.72 (±0.01)	5 (0)	0.0023 (0)	
	10	0.9 (±0.1)	3.17 (±0.01)	-3 (0)	0.0014 (0)	8.8
		4.2 (±0.2)	3.72 (±0.01)	5 (0)	0.0023 (0)	
	11	0.9 (±0.2)	3.16 (±0.01)	-3 (0)	0.0014 (0)	8.8
		3.8 (±0.3)	3.71 (±0.01)	5 (0)	0.0023 (0)	
	14					
SnO_2		2.0 (0)	3.16 (0)	-3 (0)	0.0014 (0)	7.8
		8.0 (0)	3.73 (±0.01)	5 (0)	0.0023 (0)	

k range/ 10 Å^{-1} is $2.3 \leq k \leq 14.4$; r range/ Å^{-1} is $2.2 \leq r \leq 4.0$; fitting space is back k space.

Table 5. Binding energies for Pt 4f and Sn 3d (XPS) of Pt/SnO_2 and SnO_2. The ratio of each energy is given with respect to Pt $4f_{7/2}$.

Pt concentration / at%		Binding energy (eV)					
		Pt $4f_{7/2}$				Sn $3d_{5/2}$	O 1s
Pt/SnO_2	5	75.2	85%	73.0	15%	486.8	530.6
	7	75.2	83%	73.0	17%	486.8	530.6
	9	75.2	87%	73.0	13%	486.7	530.6
	10	75.1	82%	73.0	18%	486.7	530.6
	11	75.0	69%	72.8	31%	486.7	530.6
	14	74.9	65%	72.9	35%	486.7	530.6
SnO_2		−		−		486.8	530.6

Figure 1. CH_4 (open circle) and H_2 (open square) conversions over Pt/SnO_2 films with various Pt contents. White line peak height (WLH) of Pt L_3-edge near EXAFS (filled triangles) determined from Figure 7 in order to clarify the relation between WLH and activities; the WLH of PtO_2 was 2.1.

Figure 2. Electrical resistance of 9 at% Pt-doped SnO_2 and SnO_2 as a function of hydrogen (triangles) and methane (circles) concentration, Filled and open symbols are corresponding to Pt-doped SnO_2 and SnO_2, respectively. The temperature was 723 K.

Figure 3. (a) is XRD patterns for Pt/SnO_2 with various Pt loading and SnO_2. Panel (b) shows the (101) peaks for 5 and 9 at% Pt/SnO_2.

Figure 4. Dependence of the lattice parameters along (a) *a*-axis and (b) *c*-axis on the various Pt contents.

Figure 5. Sn K-edge XANES spectra of Pt/SnO_2 together with those of reference compounds SnO_2, SnO, Sn-foil, Sn in PtSn alloy (37 wt% Pt in alloy).

Figure 6. **(a)** XANES spectra for SnO_2, 9 at% and 14 at% Pt/SnO_2, and (b) the Sn K-edge for Pt/SnO_2 films with various Pt loading.

Figure 7. (a) Pt L_3-edge XANES spectra of 7 and 9 at% Pt/SnO_2, PtO_2, PtSn alloy, and Pt foil. (b) Magnified spectra around the white lines of PtO_2 (diamonds, broken line), 5 at% (crosses, solid line), 9 at% (triangles, solid line), and 14 at% (solid line) Pt/SnO_2 samples.

Figure 8. (a) Sn K-edge k^3-weighted EXAFS oscillations ($k^3\chi(k)$) and (b) their Fourier transforms. From bottom 9 at % Pt/SnO_2, SnO_2, SnO, PtSn alloy, Sn-foil

Figure 9. Sn K-edge EXAFS spectra of Pt/SnO_2 with various Pt loading. (a) k^3-weighted EXAFS oscillations ($k^3\chi(k)$), and (b) their Fourier transforms. From bottom 5 at%, 7 at%, 9 at%, 10 at%,: 11 at%, 14 at%.

Figure 10. (a) Pt L_3-edge EXAFS oscillations, and (b) their Fourier transforms From bottom 9 at % Pt/SnO_2, PtO_2, PtSn alloy, Pt-foil.

Figure 11. Pt L_3-edge EXAFS spectra for Pt/SnO_2 with various Pt loading. (a) k^3-weighted $\chi(k)$ EXAFS oscillations, and (b) their Fourier transforms. From bottom 5 at%, 7 at%, 9 at%, 10 at%, 11 at%, 14 at%

Figure 12. XPS spectra for SnO_2 and Pt/SnO_2. (a) O 1s, (b) Sn 3d, and (c) Pt 4f.
1: SnO_2, 2: 5 at%, 3: 7 at%, 4: 9 at%, 5: 10 at%, 6: 11 at%, 7: 14 at%.

Figure 13. XPS curve fitting result for Pt 4f of a) 5 at% Pt/SnO_2, and b) 14 at % Pt/SnO_2. Blue and purple lines represent Pt^{2+} and Pt^{4+} components. Black and red lines indicate the observed and synthesized XPS spectra. Red dotted line with blue smooth line in the bottom are the residual after the fitting and smooth background, respectively.

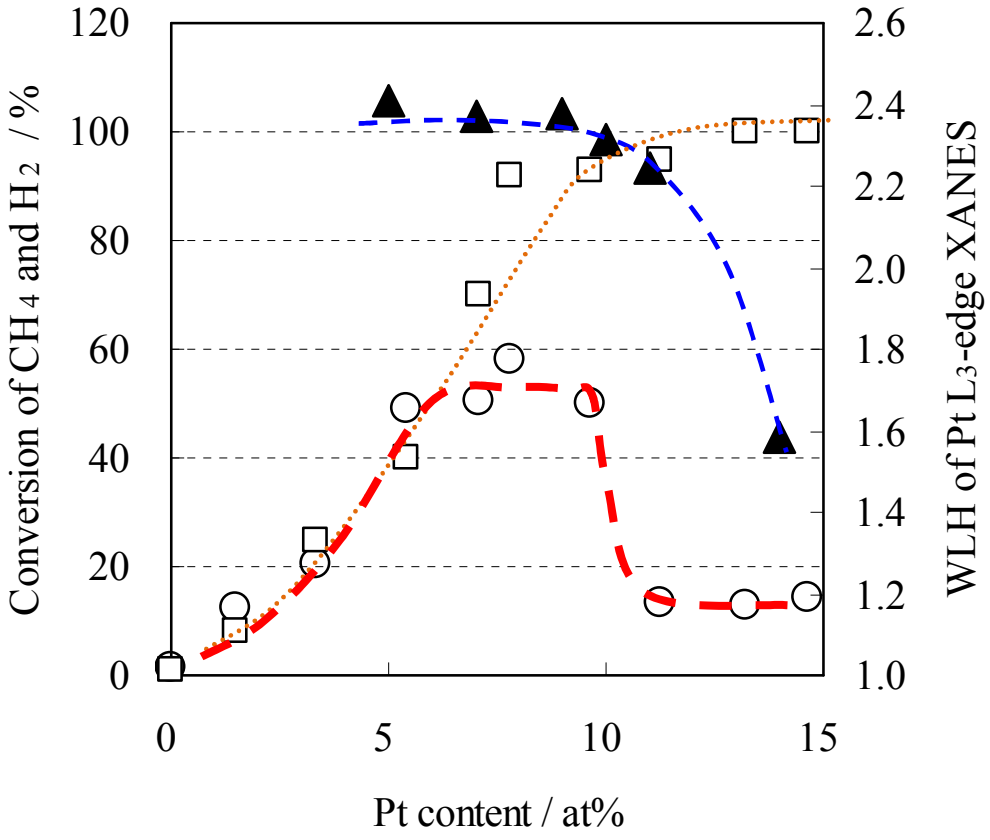

Figure 1. CH_4 (open circle) and H_2 (open squre) conversions over Pt/SnO_2 films with various Pt content. White line peak height (WLH) of Pt L_3-edge near EXAFS (close triangles) determined from Figure 7 in order to clarify the relation between WLH and activity.; the WLH of PtO_2 was 2.1.

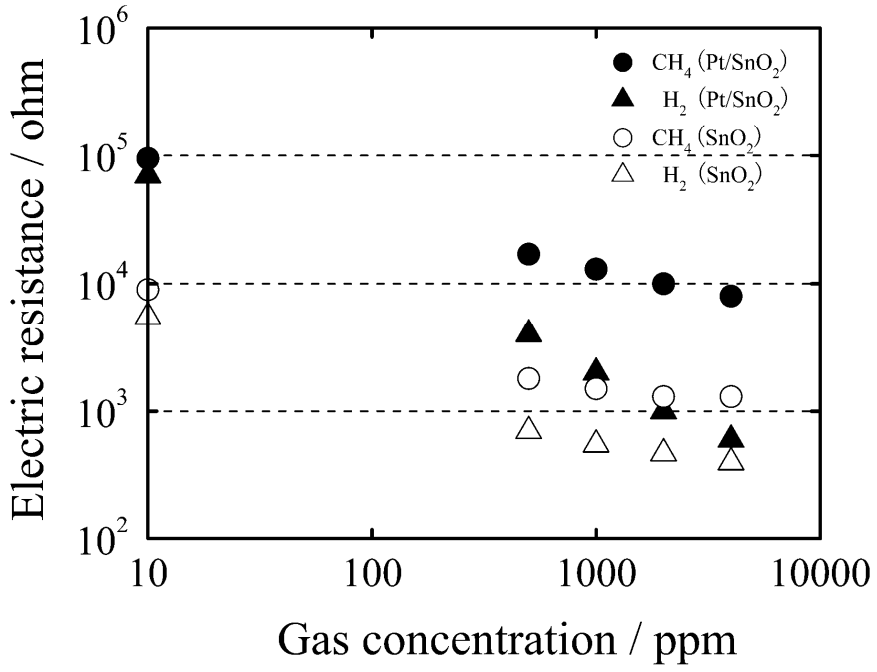

Figure 2. Electrical resistance of 9 at% Pt-doped SnO_2 and SnO_2 as a function of hydrogen (triangles) and methane (circles) concentration, Filled and open symbols are corresponding to Pt-doped SnO_2 and SnO_2, respectively. The temperature was 723K.

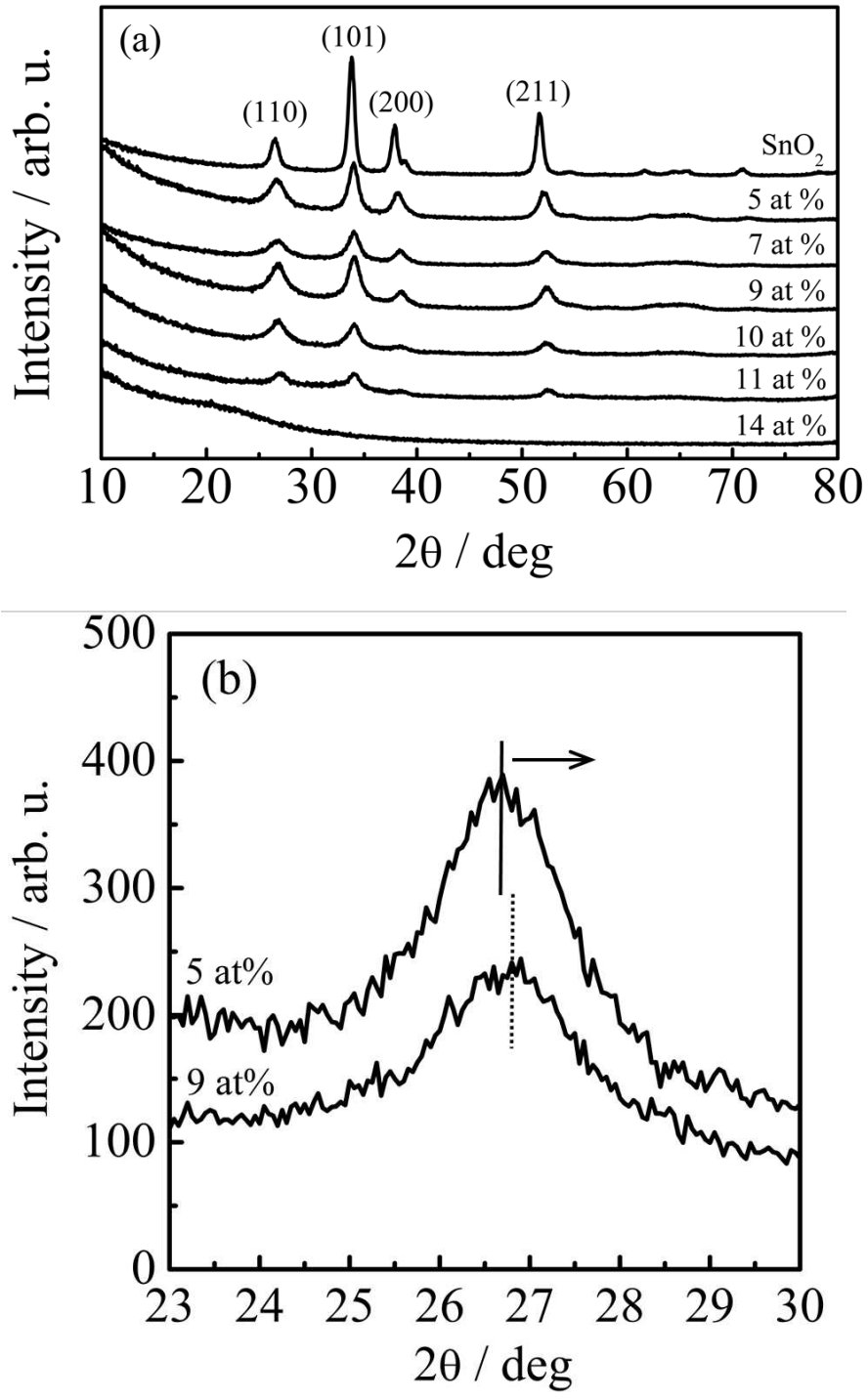

Figure 3. (a) is XRD patterns for Pt/SnO_2 with various Pt loading and SnO_2. Panel (b) shows the (101) peaks for 5 and 9 at% Pt/SnO_2.

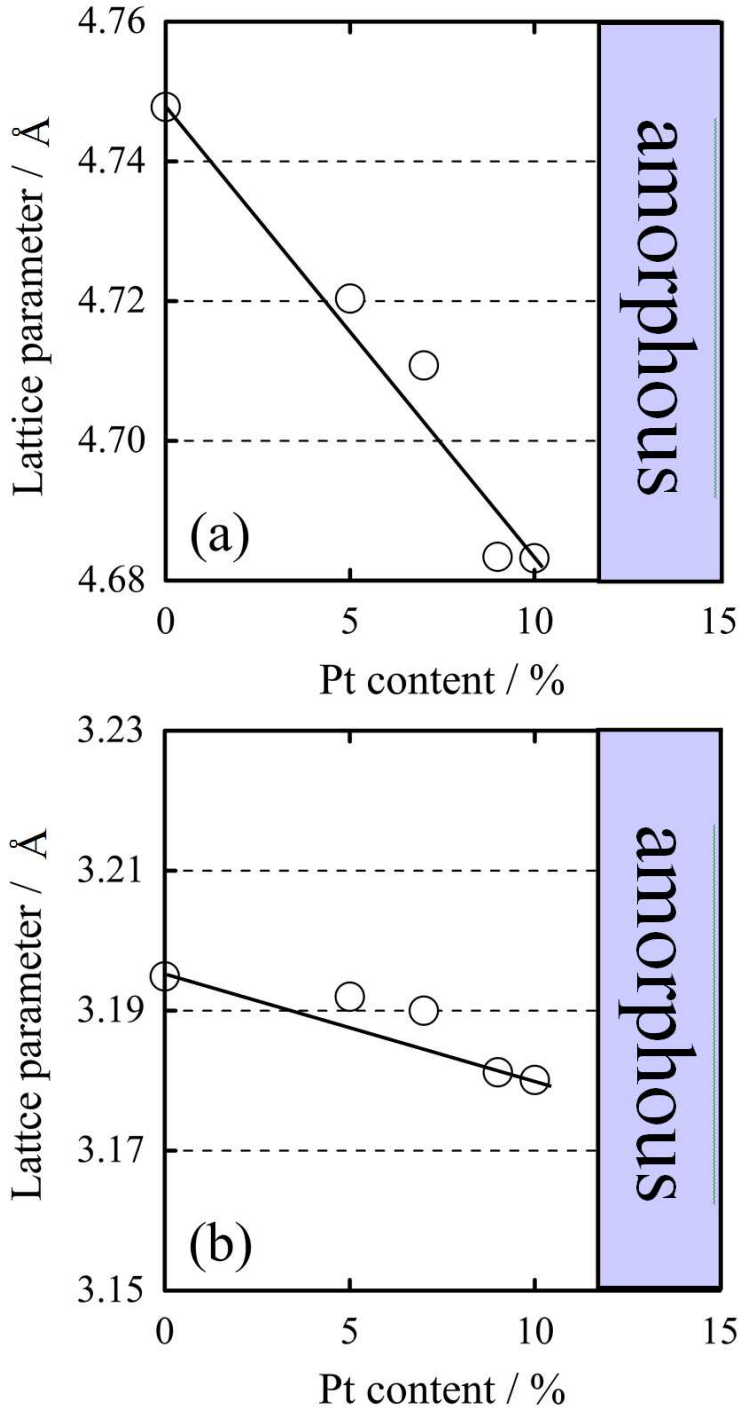

Figure 4. Dependence of the lattice parameters along (a) *a*-axis and (b) *c*-axis on the various Pt contents.

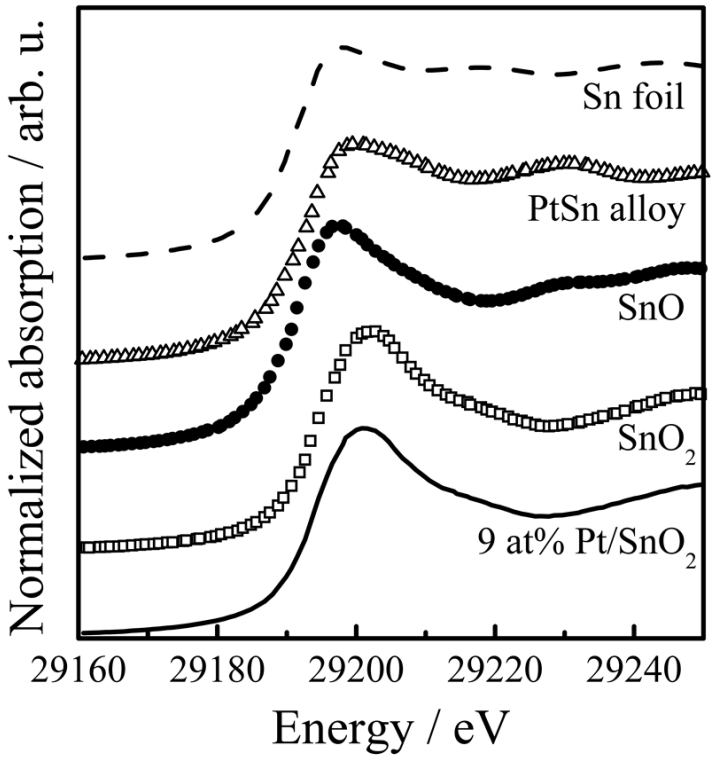

Figure 5. Sn K-edge XANES spectra of Pt/SnO_2 together with those of reference compounds SnO_2, SnO, Sn-foil, Sn in PtSn alloy (37 wt% Pt in alloy).

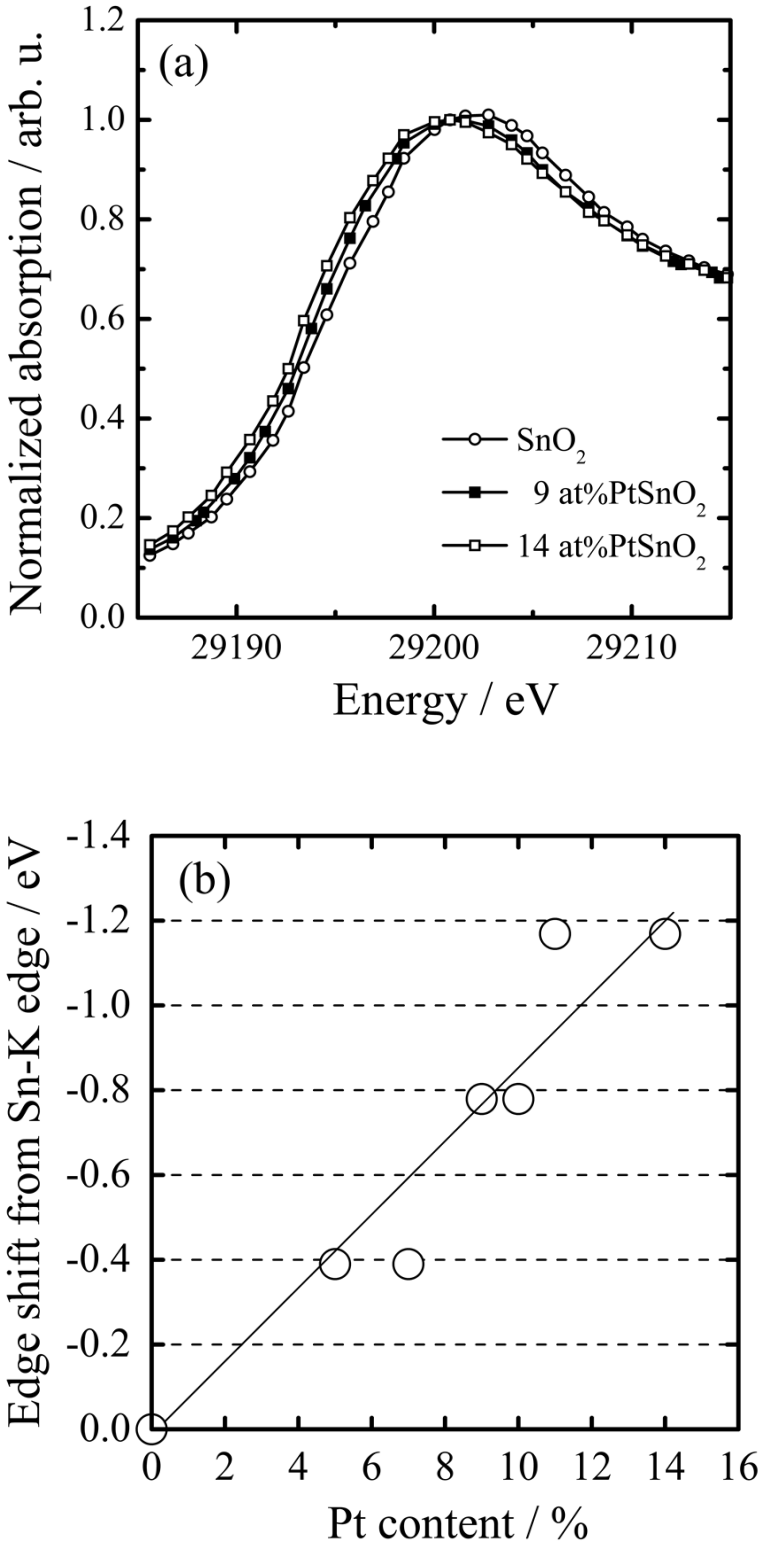

Figure 6. **(a)** XANES spectra for SnO_2, 9 at% and 14 at% Pt/SnO_2, and (b) the Sn K-edge for Pt/SnO_2 films with various Pt loading.

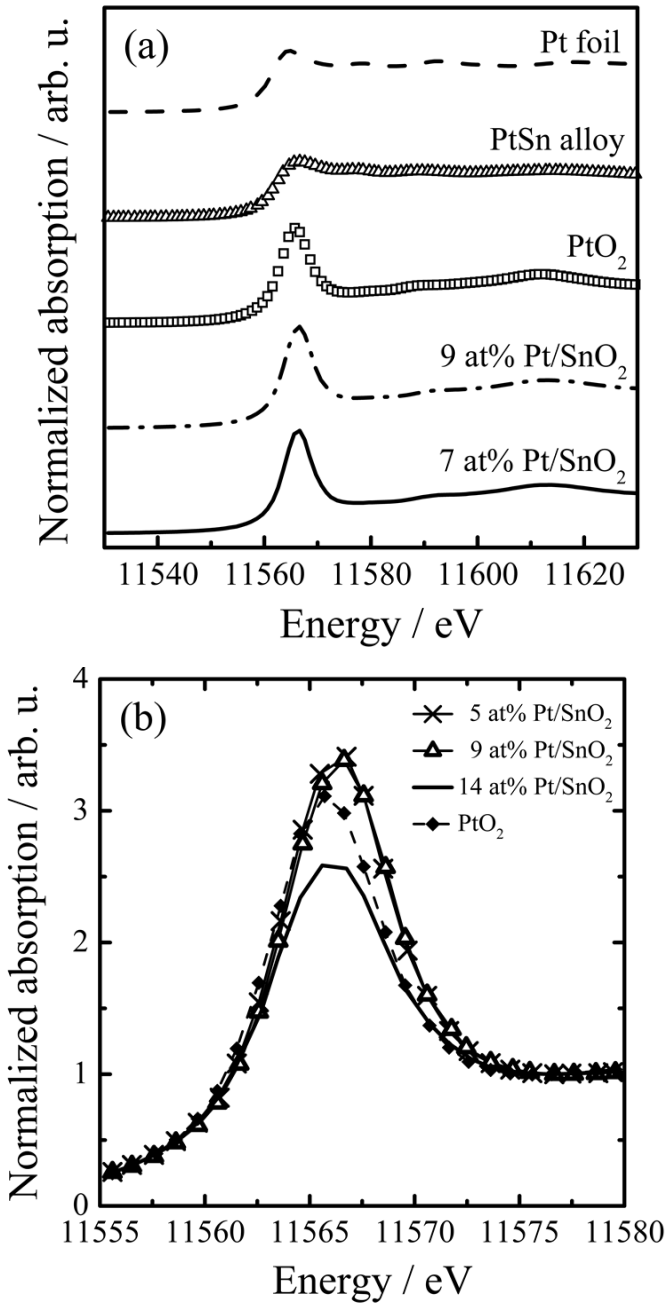

Figure 7 (a) Pt L_3-edge XANES spectra of 7 and 9 at% Pt/SnO_2, PtO_2, PtSn alloy, and Pt foil. (b) Magnified spectra around the white lines of PtO_2 (diamonds, broken line), 5 at% (crosses, solid line), 9 at% (triangles, solid line), and 14 at% (solid line) Pt/SnO_2 samples.

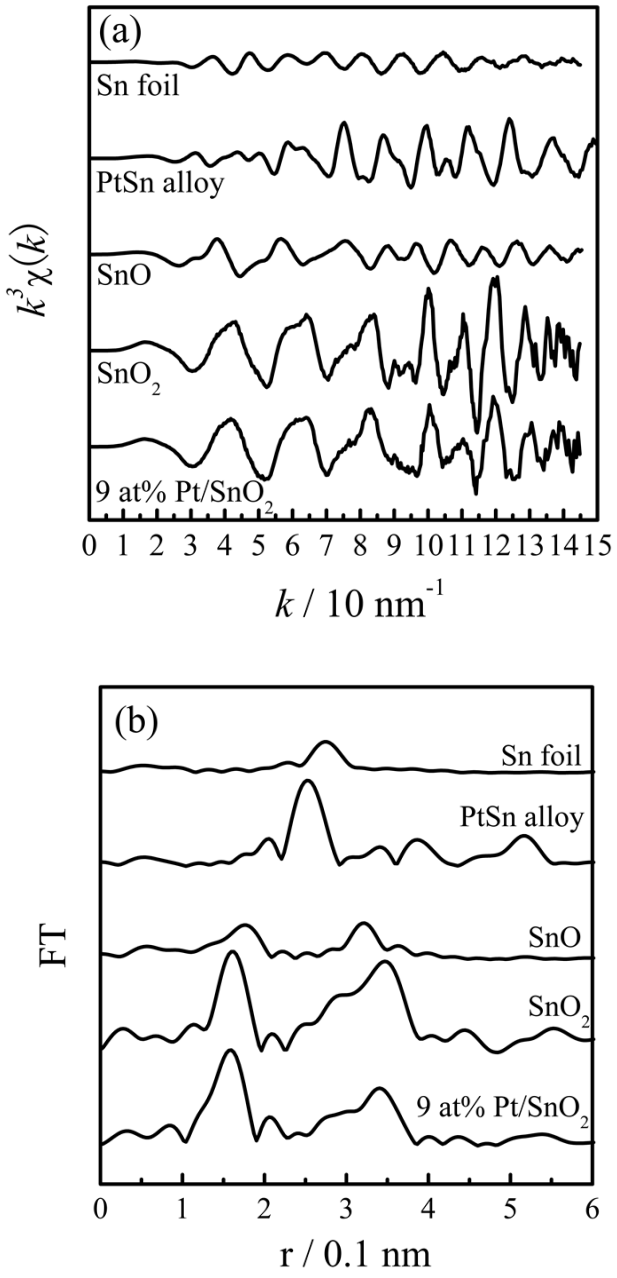

Figure 8. (a) Sn K-edge k^3-weighted EXAFS oscillations ($k^3\chi(k)$) and (b) their Fourier transforms From bottom 9 at % Pt/SnO_2, SnO_2, SnO, PtSn alloy, Sn-foil

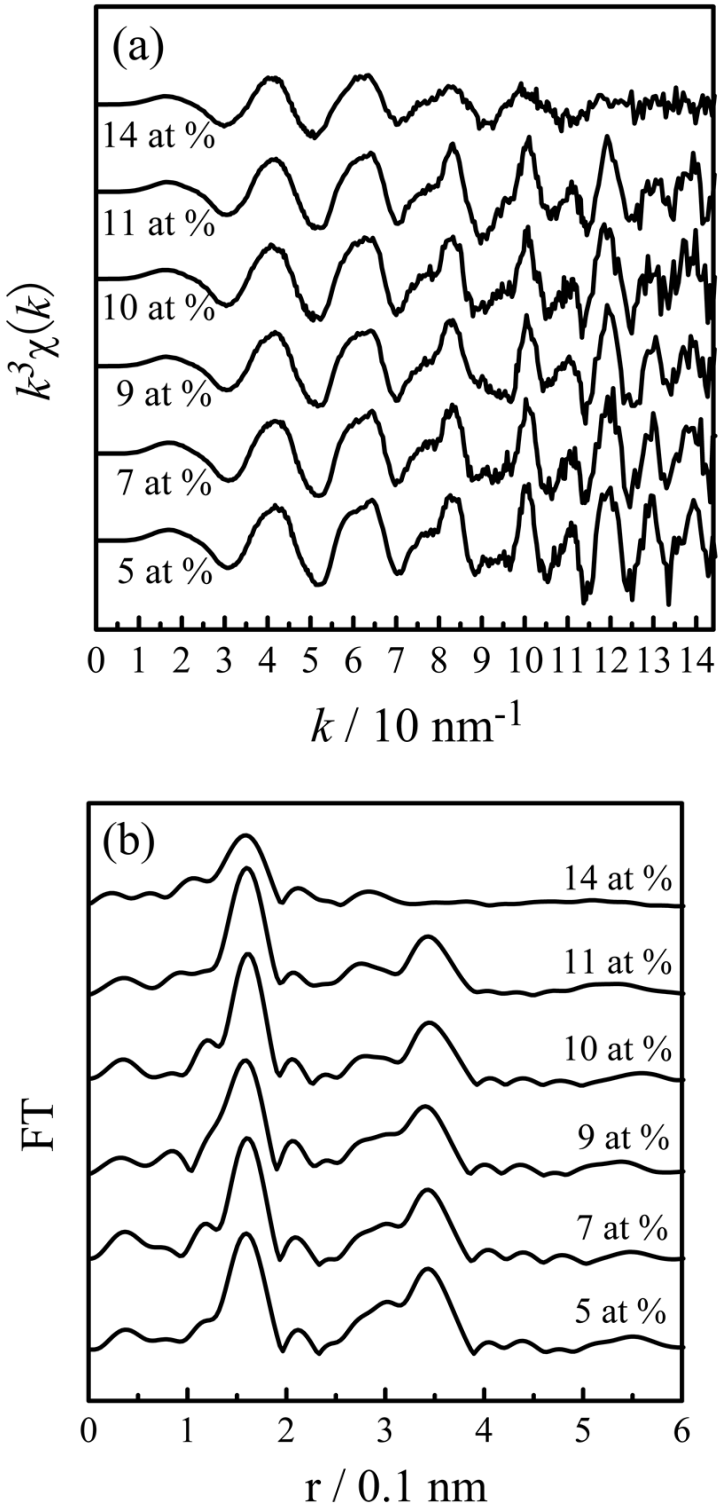

Figure 9. Sn K-edge EXAFS spectra of Pt/SnO_2 with various Pt loading. (a) k^3-weighted EXAFS oscillations ($k^3\chi(k)$), and (b) their Fourier transforms. From bottom 5 at%, 7 at%, 9 at%, 10 at%,: 11 at%, 14 at%.

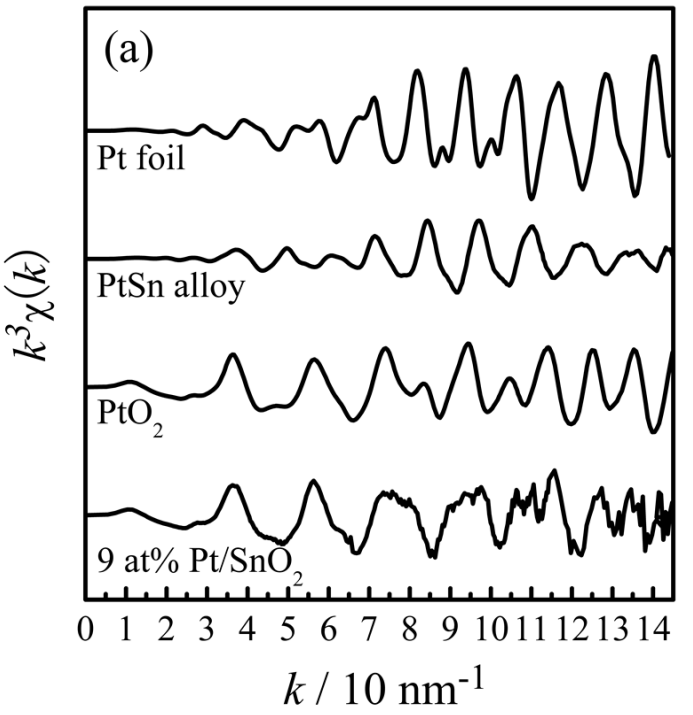

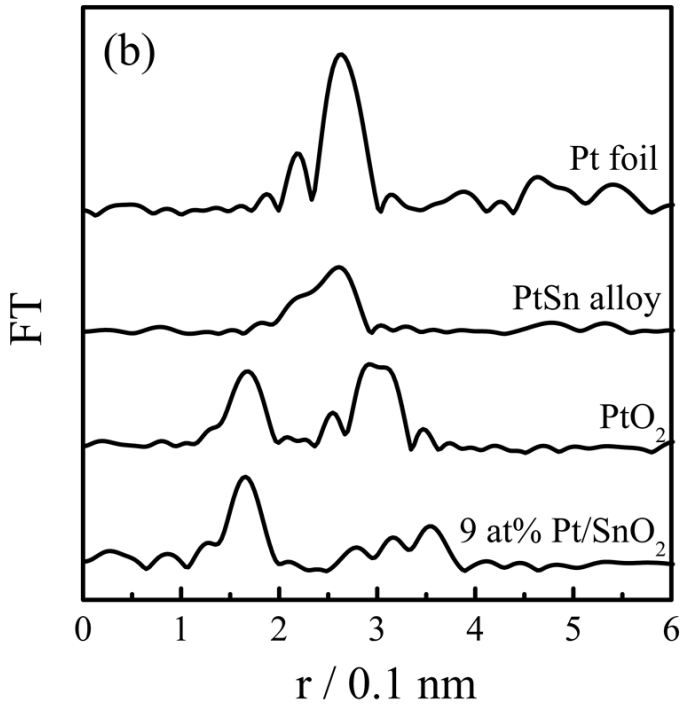

Figure 10. (a) Pt L_3-edge EXAFS oscillations, and (b) their Fourier transforms From bottom 9 at % Pt/SnO_2, PtO_2, PtSn alloy, Pt-foil.

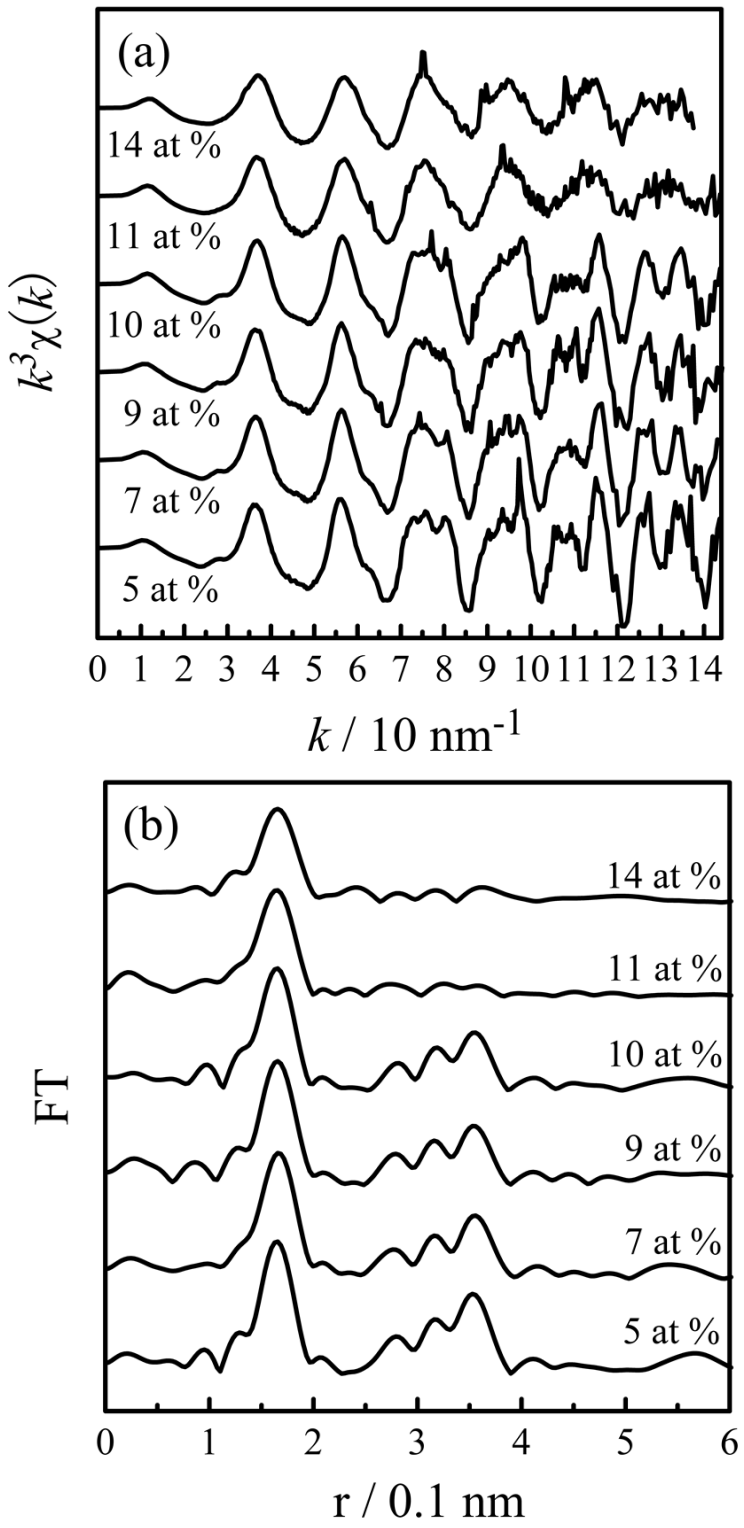

Figure 11. Pt L_3-edge EXAFS spectra for Pt/SnO_2 with various Pt loading. (a) k^3-weighted χ(k) EXAFS oscillations, and (b) their Fourier transforms. From bottom 5 at%, 7 at%, 9 at%, 10 at%, 11 at%, 14 at%

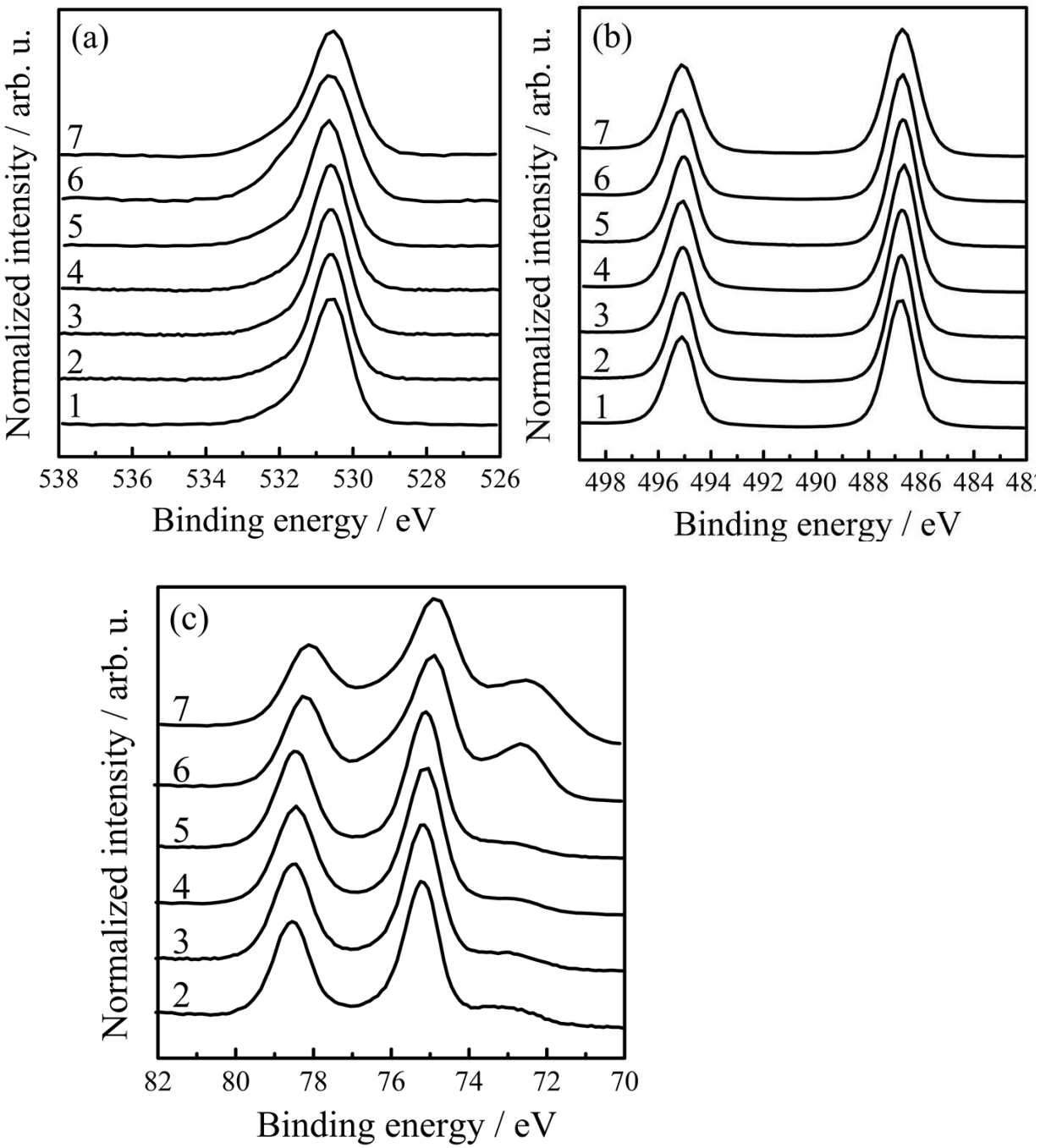

Figure 12. XPS spectra for SnO_2 and Pt/SnO_2. (a) O 1s, (b) Sn 3d, and (c) Pt 4f. 1: SnO_2, 2: 5 at%, 3: 7 at%, 4: 9 at%, 5: 10 at%, 6: 11 at%, 7: 14 at%.

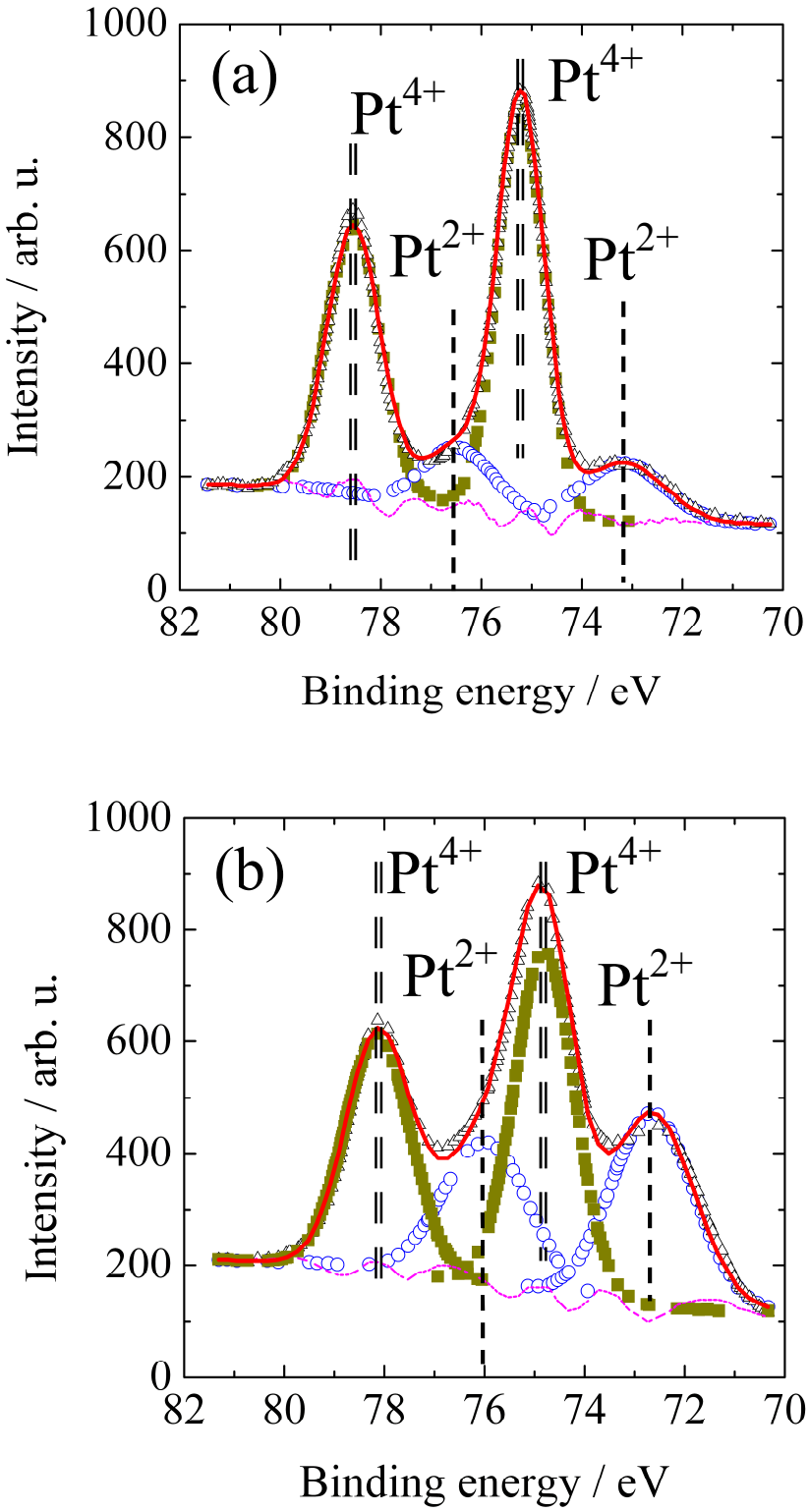

Figure 13. XPS curve fitting result for Pt 4f of a) 5 at% Pt/SnO_2, and b) 14 at % Pt/SnO_2. Open circle (Blue) and close square (green) represent Pt^{2+} and Pt^{4+} components. Open triangle (Black) and red line indicate the observed and synthesized XPS spectra. Pink dotted line with blue smooth line in the bottom are the residual after the fitting and smooth background, respectively.